Noname manuscript No.
(will be inserted by the editor)

Dispersion of tracers in the stable atmosphere of a valley opening onto a plain

Julian Quimbayo-Duarte · Chantal Staquet · Charles Chemel · Gabriele Arduini

Received: DD Month YEAR / Accepted: DD Month YEAR

Abstract We quantify the impact of a valley-wind system on the transport of passive tracers in the stably-stratified atmosphere of a valley dynamically decoupled from the atmosphere above. The simple configuration of an idealized Alpine-type valley opening onto a plain is considered, for two values of the initial buoyancy frequency and of the valley steepness. The valley-wind system consists of thermally-driven downslope flows that induce a pressure difference between the valley interior and the plain, thereby triggering a down-valley flow. A steady-state regime is eventually reached, at the beginning of which passive tracers are emitted at the valley floor and at different heights above it. The tracer emitted at the valley floor is fully mixed below the height of the maximum speed of the down-valley flow, which behaves like a jet, and remains decoupled from the tracers emitted above. The down-valley flow increases linearly in the along-valley direction y so that, from the conservation of the tracer flux, the tracer concentration decays as $1/y$. A simple theoretical model is proposed to fully account for the down-valley flow and tracer behaviours. The tracer concentration emitted at the valley floor also displays marked oscillations, which are induced by internal gravity waves radiated via a hydraulic-jump process when the downslope flow reaches the valley floor. The amplitude of the oscillations can be as high as 50% of their mean value, implying that averaged values in an urbanized valley may disguise high instantaneous – and potentially harmful – values.

Keywords Idealized Alpine valley · Numerical modelling · Passive tracer transport · Stable conditions · Valley-wind system

J. Quimbayo-Duarte · C. Staquet
Univ. Grenoble Alpes, CNRS, Grenoble INP, LEGI, 38000 Grenoble, France.
E-mail: Chantal.Staquet@univ-grenoble-alpes.fr

C. Chemel
National Centre for Atmospheric Science (NCAS), Centre for Atmospheric & Instrumentation Research
University of Hertfordshire, College Lane, Hatfield, AL10 9AB, UK.

G. Arduini
Univ. Grenoble Alpes, CNRS, Grenoble INP, LEGI, 38000 Grenoble, France
Centre for Atmospheric & Instrumentation Research, University of Hertfordshire, College Lane, Hatfield, AL10 9AB, UK.
Present address: European Centre for Medium-Range Weather Forecasts (ECMWF), Reading, Berkshire RG2 9AX, UK.

1 Introduction

Under weak synoptic flow, the airflow close to the ground in mountainous areas is driven by thermal winds. These flows develop at sunset in response to the radiative cooling of the ground and in the morning due to ground heating, being downslope and upslope, respectively. During wintertime, downslope flows dominate due to the lower insolation and more pronounced shadowing effects (Largeron and Staquet 2016). These flows lead to the formation of cold-air pools in valleys, whose role in trapping air pollution has been well-documented (Silcox et al. 2012, Whiteman et al. 2014). Therefore, under a wintertime anticyclonic regime, urbanized valleys always experience high air pollution levels (Brulfert et al. 2005), particularly for PM_{10} (particulate matter of aerodynamical diameter smaller than 10 μm). When the anticyclonic regime persists for several days, as is common, the thermal structure within the valley eventually displays a vertical temperature gradient of positive sign (referred to as an inversion layer) extending throughout the valley depth. These inversion layers are persistent during the whole anticyclonic period, apart from the region immediately above the ground, which can be eroded due to convection around midday. Thermal stratification and thermally-driven flows are therefore determinant in controlling the distribution of pollutants, once emitted, in the atmosphere of a valley under wintertime anticyclonic conditions.

While the formation, persistence and destruction of inversion layers, along with the associated evolution of thermally-driven winds, have been examined in several studies, both using data from field campaigns (e.g. Whiteman et al. 2004, Lareau et al. 2013) and from numerical modelling (e.g. Largeron and Staquet 2016), their impact on pollutant transport has received less attention. When the pollutant is considered to be passive, as is assumed to be valid for PM_{10} herein, computations of mass fluxes already provide useful pointers on the fate of pollutants. However, what matters at a given site is the spatial distribution of pollutants and how the thermal and wind structure control that distribution. A specific study involving passive tracer transport is required for this purpose. This is the aim of the present work, using numerical modelling of a three-dimensional idealized valley.

Previous numerical modelling studies aiming at relating the atmospheric dynamics and passive tracer transport in mountainous terrain were first conducted by considering a quasi two-dimensional valley, namely with no change along the valley axis. Anquetin et al. (1999) presented results describing the influence of seasonal variations (summertime and wintertime) on the mechanisms responsible for inversion layers, and their consequences on pollutant trapping within valleys. Chemel and Burns (2015) investigated the transport and mixing of pollutants into the stable atmosphere of a valley when the emission sources are located along the slopes. The authors noted that downslope flows transport pollutants into the valley to depths that depend on the temperature deficit of the downslope flows. Rendón et al. (2014) showed that, when a temperature inversion is present, the warming associated with the heat island created by urban areas affects the concentration field of passive tracers by accelerating the break-up of the temperature inversion. Lang et al. (2015) investigated daytime air pollution over complex terrain in a set of two parallel valleys (i.e. three parallel ridges) of varying valley-floor altitude in the cross-valley direction. Results showed that the differences in thermally-driven flows and their impact on tracer transport are highly sensitive to the difference in altitude of the different valley floors.

Because the valley geometry was two-dimensional in these studies, the role of the along-valley flow on pollutant transport could not be examined. Three-dimensional idealized topographies were considered recently in a few numerical modelling studies. Wagner et al. (2014) considered a valley in between two ridges opening onto a plain for daytime convective conditions. The analysis of mass-flux budgets and forward trajectories indicated that mass is transported three to four times more effectively from the surface to the free atmosphere over valleys than over flat terrain and that vertical transport is greater for deep and narrow valleys. Lehner and Gohm (2010) performed numerical simulations using both two- and three-dimensional terrain configurations to investigate the influence of vertical inhomogeneities in the thermal stratification and vegetation cover on slope-wind circulations and tracer transport. The authors concluded that the increase in the albedo causes a reduction of the mass flux in the slope flow, directly affecting tracer transport. Cuxart and Jiménez (2007) used a three-dimensional numerical model to simulate a low-level jet developing over a gentle slope, based on field observations from the SABLES-98 field campaign over the northern Spanish plateau. The model was able to reproduce the two-layer structure of the jet observed during the campaign. This jet structure consists of two turbulent layers separated by a change of the temperature gradient at the height where the jet maximum is located. A passive tracer was used to track the mass exchange between the two layers, leading to the conclusion that it is very small.

The present work relies on three-dimensional numerical simulations of an idealized Alpine-type valley opening onto a plain for wintertime stable atmospheric conditions. It is based on Arduini et al. (2016) who considered the same valley configuration for one set of the physical parameters and no passive tracer. The main objective is to characterize the role of downslope and down-valley flows on the transport of passive tracers released at different locations, both on the valley floor and above it. The numerical set-up is presented in Sect. 2. The dynamics of the downslope and down-valley flows are reported in Sect. 3 and their impact on passive tracer transport is discussed in Sect. 4. A summary and conclusions are given in Sect. 5.

2 Methods

2.1 Numerical Model

We use the Weather Research and Forecasting (WRF) numerical model (Peckham et al., 2012), version 3.4.1, which is a fully compressible, non-hydrostatic model that uses a hydrostatic pressure terrain-following vertical coordinate and a staggered grid of Arakawa-C type. The model was run using a large-eddy simulation (LES) configuration. The LES formulation computes the large-scale turbulent motions by solving the filtered three-dimensional Navier–Stokes equations, while the small-scale motions are parametrized using a subgrid-scale (SGS) model. The 1.5-order turbulent kinetic energy closure of Deardorff (1980) was used to model these SGS motions, with the modification proposed by Scotti et al. (1993) to account for the strong anisotropy of the grid along the slope close to the ground. The WRF model is coupled with a chemistry module (WRF-Chem), which is capable of simulating the transport, mixing and chemical transformation of trace gases and aerosols. In the present case, only the transport of passive tracers is considered.

2.2 Topography of the Valley

The topography is an idealized U-shape valley opening onto a plain (see Fig. 1a). All points have been assigned the geographical coordinates of 45.92°N and 6.87°E, a position located in the Chamonix valley, a typical valley in the French Northern Alps. The idealized valley is oriented south–north, along the y-direction. The topography is similar to that proposed by Rampanelli et al. (2004), which is symmetric with respect to the vertical plane $y = 0$ to facilitate the implementation of the boundary conditions on the north and south sides. Only the southern half of the domain will be considered. In the following, the *beginning of the valley* refers to the $y = 0$ plane. The analytical expression for the height of the terrain is given by

$$h(x,y) = H\, h_x(x)\, h_y(y) + h_0, \tag{1}$$

where

$$h_x(x) = \begin{cases} \left[1 - \cos\left(\pi\left(|x| - L_x\right)/S_x\right)\right]/2 & \text{for} \quad L_x \le |x| \le S_x + L_x \\ 0 & \text{for} \quad |x| < L_x \\ 1 & \text{for} \quad |x| > S_x + L_x \end{cases} \tag{2}$$

and

$$h_y(y) = \begin{cases} \left[1 + \cos\left(\pi\left(|y| - L_y\right)/S_y\right)\right]/2 & \text{for} \quad L_y < |y| \le S_y + L_y \\ 0 & \text{for} \quad |y| > L_y + S_y \\ 1 & \text{for} \quad |y| \le L_y \end{cases} . \tag{3}$$

The valley depth H is equal to 800 m, which is also the altitude above the valley floor of the plateaux extending symmetrically on both sides of the valley in the cross-valley direction x (Fig. 1a). The length of the valley in the along-valley direction L_y is equal to 6 km and, together with the length of the sloping sidewall in that direction $S_y = 5$ km, the total length of the valley is equal to 11 km (Fig. 1b). The position where the plain starts is referred to as *the valley exit*. The valley floor half-width is equal to $L_x = 720$ m (in the cross-valley direction x) and is set at $h_0 = 1000$ m above sea level (a.s.l.).

Two topographies are considered, only differing in the steepness and length of the sloping sidewall in the cross-valley direction S_x. For the first topography, referred to as T1, the maximum slope angle is 16.7° and $S_x = 4200$ m. This is the topography considered in Arduini et al. (2016). For the second topography, denoted T2, the maximum slope angle is 8.3° and $S_x = 8600$ m (Fig. 1c).

2.3 Initial Conditions

The numerical simulations use a stable atmosphere, starting one hour before sunset on a winter day (21 December) and lasting either 6 or 8 h. At the initial time, the vertical gradient of the (virtual) potential temperature profile $\partial\theta_v/\partial z$ is constant and no flow imposed. Therefore, the atmosphere of a winter night under decoupled conditions with the synoptic flow is simulated. A relatively dry atmosphere is considered using a constant relative humidity value of 40% at the initial time. Two values of the initial stratification are considered, either $\partial\theta_v/\partial z = 1.5$ K km^{-1} associated with the buoyancy frequency $N_1 = 0.00715$ s^{-1}, or $\partial\theta_v/\partial z = 6$ K km^{-1} associated with $N_2 = 0.01430$ s^{-1}; the buoyancy (or Brunt-Väisälä) frequency is defined by $N^2 = (g/\theta_{v,ref})\partial\theta_v/\partial z$, where g is the acceleration due to gravity and $\theta_{v,ref} = 288$ K is a reference temperature, equal to the near-surface temperature at the initial time. This value can be considered as a typical temperature at that time of the year in the French Alps. Burns and Chemel (2014) conducted a brief study to estimate the near-surface temperature in the area of the Chamonix valley during one week in January 2003. The near-surface temperature (at 2 m above the ground level) at 1600 local time consistently showed a value of the virtual potential temperature close to 288 K (namely 279.3 K for the associated potential temperature, for a relative humidity of 40%), which accounts for the value of $\theta_{v,ref}$ in the present set of simulations.

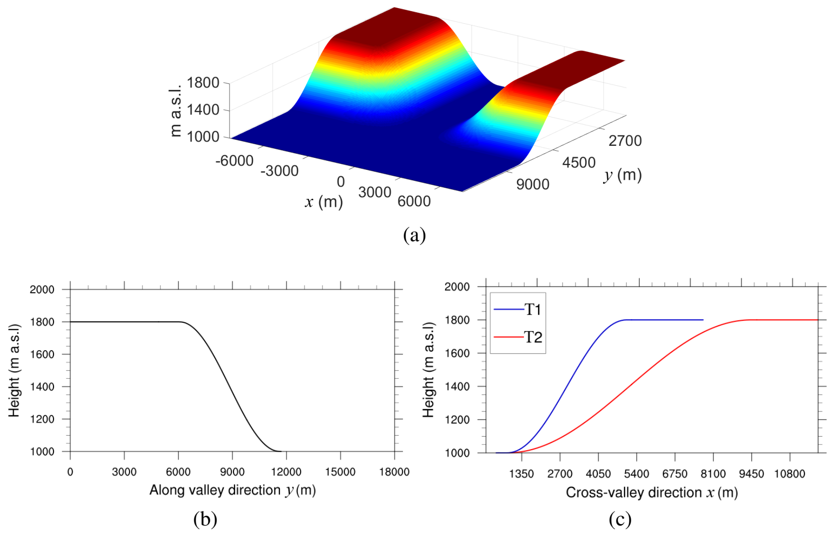

Fig. 1 a) Three-dimensional view of topography T1. b) Terrain height in the along-valley direction at $x = 7$ km from the valley centre. c) Terrain height in the cross-valley direction for $0 \leq y \leq 6$ km, for T1 and T2. The numerical domain is symmetric with respect to the plane $y = 0$ and only its southern part ($y \geq 0$) is displayed in frames a) and b).

Three numerical simulations have been performed, different in either the topography (T1 or T2) or the initial stratification (N_1 or N_2). In simulation S1, topography T1 is used with stratification N_1; simulation S2 differs from S1 through the topography, which is T2; simulation S3 differs from S1 through the buoyancy frequency, which is N_2 (see Table 1). In Arduini et al. (2016) only simulation S1 was considered (and the modification of the SGS model proposed by Scotti et al. (1993) was not implemented).

Simulations							
Sim.	Topo	Slope length (m)	Max slope ang. (°)	$\partial\theta_v/\partial z$ (K km^{-1})	N (rad s^{-1})	Grid pts (x)	Grid pts (y)
S1	T1	4200	8.3	1.5	7.15×10^{-3}	172	361
S2	T2	8600	16.7	1.5	7.15×10^{-3}	270	361
S3	T1	4200	8.3	6	1.43×10^{-2}	172	361

Table 1 Main parameters of the simulations. The number of grid points indicated is that of the inner domain, the horizontal resolution being 90 m. In the outer domain, the horizontal resolution is set to 270 m.

2.4 Boundary Conditions

All simulations were run in a one-way nested domain configuration using two domains. In the outer domain, periodic boundary conditions are imposed at the east and west boundaries. On the east and west sides of the valley, the plateaux are long enough (3000 m) to prevent the influence of these boundary conditions on the inner domain. As for the boundaries in the y-direction, open boundary conditions are imposed at the north and south boundaries of the outer domain, thanks to the symmetry with respect to the plane $y = 0$ of T1 and T2. In the inner domain, the boundary conditions are provided by the fields computed in the outer domain and are updated every outer-domain timestep. No information passes from the inner to the outer domain due to the one-way nesting.

To prevent wave reflection at the top of the domain, located at 12 km a.s.l., a Rayleigh damping layer (Klemp et al., 2008) is set using a damping depth equal to 4000 m and a damping coefficient equal to 0.2 s^{-1}. At the ground the usual impermeability condition is used. The atmospheric surface-layer is modelled by the revised MM5 Monin–Obukhov surface-layer scheme proposed by Jiménez et al. (2012); it provides in particular the bottom boundary conditions for the turbulent fluxes. Radiative transfer is considered using the Rapid Radiative Transfer Model for longwave radiation (Mlawer et al., 1997) and the scheme proposed by Dudhia (1989) for shortwave radiation. The soil type is "silty clay loam", which is consistent with the typical Alpine valley landscape in the absence of snow. The skin temperature is initialized through an extrapolation of the temperature in the first three layers above the surface.

2.5 Numerical Parameters

The size of the inner domain is 15 km × 32 km in the x- and y-directions, respectively, for T1 and 25 km × 32 km for T2, with a grid size of 90 m in both directions. The size of the domain of interest is therefore equal to 16 km in the y-direction, as discussed above. The outer domain is two times larger than the counterpart inner domain in the x-direction and three times larger in the y-direction, with a horizontal grid size of 270 m. Both domains share the same vertical discretization with 100 grid points: the first mass point is at 1.7 m above the surface and the vertical coordinate is stretched so that the first 20 m are discretized with 10 grid points and the first 100 m with 26 grid points. The timestep is equal to 0.075 s for the inner domain, and is three times larger for the outer domain. A summary of the physical and numerical parameters of simulations S1, S2 and S3 is provided in Table 1.

2.6 Initialization of the Passive Tracer

The tracers used in the present experiment are passive (with no chemical reaction), the physical properties of the tracers being those of dry air so that no deposition effect needs to be modelled. Four different emission zones (Z_i) with the same surface area are defined along the valley axis, centred at 3, 5, 7, and 9 km from the beginning of the valley (see Fig. 2). Each emission zone at ground level is replicated at four different levels above it implying that 16 tracers are emitted for each simulation. Each zone Z_i is composed of an array of 12×16 grid cells in the north–south and east–west direction, respectively, and the tracer emission is distributed in a single grid cell along the vertical. The emission rate Q over a given zone Z_i is constant in time and equal to 6.56×10^{-7} kg s^{-1}. An initial background tracer concentration is imposed in the whole domain, with value 1.25×10^{-12} $\mathrm{kg\,m^{-3}}$. Hereafter each tracer is named as $TrSn_{i,j}$, where $1 \le n \le 3$ denotes the simulation number in which the emission has been released, $1 \le i \le 4$ and $1 \le j \le 4$ refer to the area at the valley bottom and to the height at which the tracer is released, respectively (see Table 2). Tracers are released 150 min after the initial time, as justified below.

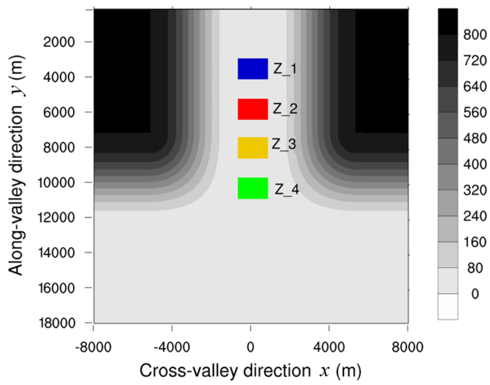

Fig. 2 Locations of the passive tracer emissions. Each colour zone (Z_i) corresponds to an emission source, all zones having the same area (1440 m x 1080 m). Four different tracers were emitted in each zone at different levels (0, 95 m, 280 m and 415 m above the ground). The contours displayed are those for topography T1.

Emission Sources				
Height above the surface (m)	Z_1 (3 km)	Z_2 (5 km)	Z_3 (7 km)	Z_4 (9 km)
0	$TrSn_{1,1}$	$TrSn_{2,1}$	$TrSn_{3,1}$	$TrSn_{4,1}$
95	$TrSn_{1,2}$	$TrSn_{2,2}$	$TrSn_{3,2}$	$TrSn_{4,2}$
280	$TrSn_{1,3}$	$TrSn_{2,3}$	$TrSn_{3,3}$	$TrSn_{4,3}$
415	$TrSn_{1,4}$	$TrSn_{2,4}$	$TrSn_{3,4}$	$TrSn_{4,4}$

Table 2 Location of the tracers released in the simulations. Each tracer is named $TrSn_{i,j}$, where $1 \leq n \leq 3$ is the simulation number, $1 \leq i \leq 4$ is the zone number on the valley bottom and $1 \leq j \leq 4$ is the height index at which the tracer is released over the valley bottom. All zones are horizontal and centred with respect to the valley axis. For $i = 1$, Z_i is also centred with respect to the position $y = 3$ km; for $i = 2$, $y = 5$ km; for $i = 3$, $y = 7$ km and for $i = 4$, $y = 9$ km. For $j = 1$, the tracer is released at the valley bottom; for $j = 2$, at 95 m above the valley bottom; for $j = 3$, at 280 m and for $j = 4$, at 415 m. The zones correspond to the colour areas Z_i in Fig. 2; each zone has an area of 1440×1080 m^2.

3 Analysis of the Valley-Wind System

The flow behaviour for the parameters of simulation S1 has been studied in detail by Arduini et al. (2016), with a focus on the impact of the valley-wind system on the development of the cold-air pool. Here, the analysis of the flow dynamics for S1 is related to the flow properties that affect the passive scalar behaviour: the oscillations of the velocity components (Sect. 3.2), the vertical structure of the cold-air pool (Sect. 3.3) and the mixing regions (Sect. 3.4). A sensitivity study is next conducted (Sect. 3.5) for a slope angle of the valley twice smaller (simulation S2) and a value of the buoyancy frequency twice larger (simulation S3).

3.1 Overall Behaviour of the Flow

During nighttime, a negative buoyant flow is detected over the valley sidewalls. The generation of this downslope flow is produced by a sign reversal in the surface radiative budget over the valley. During the day this budget has a positive sign as a result of shortwave solar radiation. On the late afternoon solar radiation decreases and is eventually overcome by longwave radiation emitted from the ground, leading to surface cooling. The sensible heat flux is then directed from the atmosphere to the ground resulting in a shallow layer of cooler air over the slope surface. This air layer is therefore denser than the air parcels located at the same altitude further away from the slope; as a result, a downslope flow develops following the valley shape.

The downslope flow speed, denoted U_s, follows a jet structure normal to the slope, with a maximum value (jet nose) reached at about 5 m above the ground in simulation S1 (not shown). Time series of U_s are presented in Fig. 3a for S1 at different positions along the valley axis, at a height of 5 m above the ground and for x = 2000 m (close to the bottom of the slope). Fig. 3a shows that U_s develops within the first hour with a growth rate almost independent of the position along the valley axis. This growth rate is controlled by radiative cooling and the stratification, which are independent of the along-valley direction. In contrast, U_s reaches a maximum value that depends on the length of the slope (which is the same at $y = 3$ and $y = 6$ km but shorter at $y = 9$ km). This maximum value is reached between 60 and 120 min, and U_s next decays and reaches a quasi-steady state.

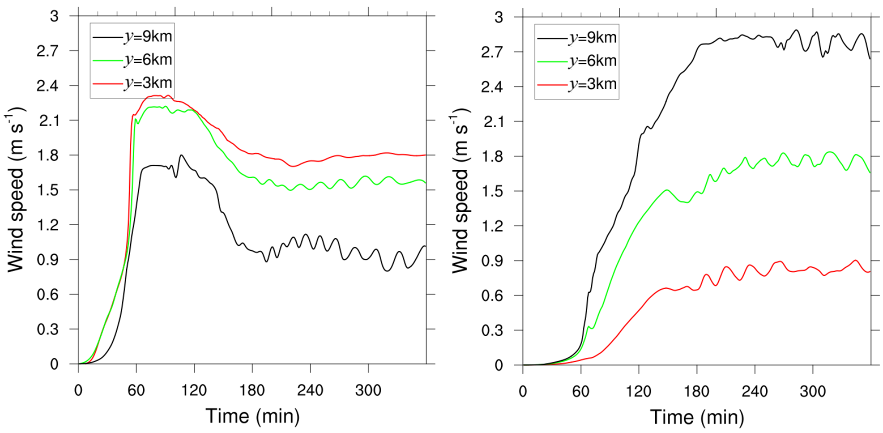

(a) (b)

Fig. 3 a) Time series of the downslope flow speed at three different locations along the valley axis. For the three locations, $x = 2000$ m and $z = 5$ m above the ground. b) Time series of the down-valley flow speed averaged over the valley bottom at 5 m above the bottom at the same three locations along the valley axis. Results are shown for simulation S1.

The advection of cold air along the slopes by the downslope flows, and subsequent upward transport from the convergence of the downslope flows at the valley centre, create a cold-air pool in the valley. The resulting temperature difference, and therefore pressure difference through hydrostatic balance, between the valley interior and the plain triggers a down-valley flow, with speed denoted V (see Fig. 3b).

As opposed to U_s, the rate at which V develops is strongly dependent on the position along the valley axis: it is larger close to the valley exit, where the pressure gradient between the valley and the plain is largest and decays as one moves towards the beginning of the valley (note that V vanishes for $y = 0$ due to the symmetry of the topography with respect to the $y = 0$ vertical plane). The down-valley flow is therefore generated at the valley exit and, by mass conservation, further develops inside the valley; this implies that a return flow should form as well at higher altitude. Consistent with its generation mechanism, this down-valley flow exists only within the cold-air pool.

The downslope and down-valley flows eventually reach a quasi-steady regime whose origin is discussed in Arduini et al. (2016). This regime is reached after 3 h, a duration that depends on the ratio of the length to the height of the valley and on the buoyancy frequency (see also Schmidli and Rotunno, 2015). Marked temporal oscillations in the time series of U_s and V are noticeable during the quasi-steady regime, which are analyzed in the next section. A simple model of the down-valley flow speed during the quasi-steady regime is proposed in Sect. 4.4.

3.2 Analysis of the Flow Oscillations

As shown in Sect. 4, the oscillations of the down-valley flow speed have an impact on the passive tracer concentration. We investigate here the origin of these oscillations, for the downslope and down-valley flows.

Energy spectra of U_s and V have been computed from the time series displayed in Fig. 3 when the quasi-steady regime is reached (see Fig. 4). The energy spectrum of U_s displays two main peaks whatever the value of the y-location along the valley axis, equal to 3.1×10^{-4} Hz and 7.3×10^{-4} Hz (owing to the resolution in frequency of the spectrum, equal to 1.04×10^{-4} Hz). Only the latter peak is convincingly detected in the spectra of the time series of V whatever the y-location.

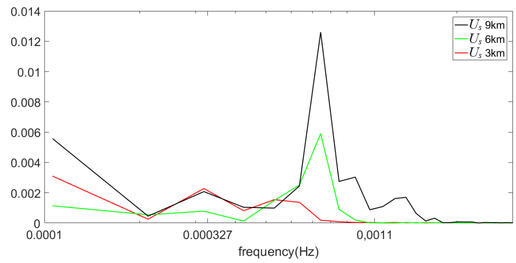

(a)

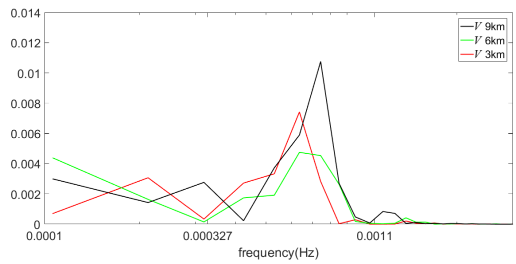

(b)

Fig. 4 a) Energy spectrum of the downslope flow speed (U_s) (a) and down-valley flow speed (V) (b) from 200 to 360 min, for the time series displayed in Fig. 3. A log-log scale is used. The frequency predicted by McNider's model, equal 3.27×10^{-4} Hz, and the buoyancy frequency, equal to 1.1×10^{-3} Hz, are indicated with tickmarks. Results are shown for simulation S1.

The smallest frequency peak can be accounted for by the combination of the effects of radiative cooling from the ground and stratification, following a simple model proposed by

McNider (1982). According to this model, valid for a constant slope of infinite extent in a uniformly stratified atmosphere, a fluid particle advected by the downslope flow oscillates at a frequency equal to $N \sin\alpha/2\pi$, where N is the (constant) value of the buoyancy frequency and α is the slope angle. Using for N the value at the initial time and for α the maximum slope angle in the y-plane the downslope flow is considered, as in Chemel et al. (2009), a value of 3.27×10^{-4} Hz is obtained for the oscillating frequency for $y = 3$ and 6 km. This value is indicated in Figs. 4a,b and matches quite well the first frequency peak for U_s. For $y = 9$ km, the maximum slope angle is lower than at $y = 3$ and 6 km, leading to a frequency value very close to the minimum frequency of the spectra, which is therefore ill-resolved. Hence, the first peak of the spectra at $y = 9$ km should not be given any physical interpretation.

The second frequency peak can be explained by relying again on the analysis of Chemel et al. (2009). It is indeed the signature of an internal gravity wave field emitted by the downslope flow when it experiences a hydraulic jump at the bottom of the slope (see also Renfrew, 2004). The period associated with this frequency is about 23 min, which matches well the period of the oscillations observed in Fig. 3. To attest that internal gravity waves with this period are indeed radiated, a (t,z) diagram of the vertical velocity component is displayed in Fig. 5 at a mid-slope location and at $y = 3$ km. A propagating internal gravity wave pattern is clearly detected, whose period is also in agreement with that associated with the second frequency peak.

We therefore conclude that the oscillations in the down-valley flow speed V result from the emission of this internal gravity wave field and that the downslope flow speed U_s is also subject to McNider's oscillations.

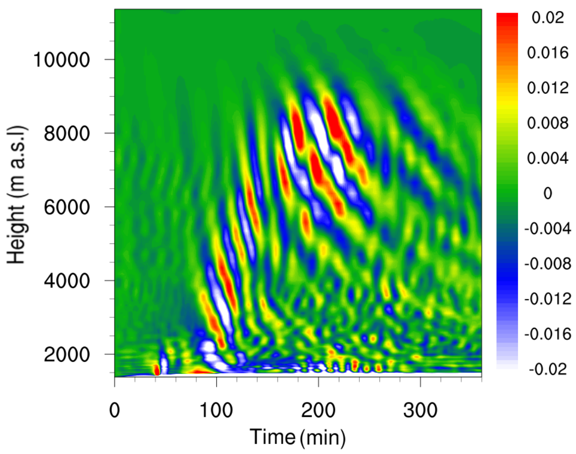

Fig. 5 (t,z) diagram of the vertical velocity component [m s^{-1}] at $x = -2850$ m (mid-slope) and $y = 3000$ m. Results are shown for simulation S1.

3.3 Vertical Profiles of the Down-Valley Flow Speed and of the Absolute Temperature Along the Valley Axis

The vertical profiles of the down-valley flow speed and of the absolute temperature, along with the counterpart buoyancy frequency, are displayed in Fig. 6 at different positions along the valley axis, at $t = 360$ min.

As shown by Arduini et al. (2016), the height of the cold-air pool created by the downslope flows (and subsequently modified by the development of the along-valley flow) decreases from the beginning of the valley to the valley exit as a result of the decreasing depth of the valley. This is also attested in Fig. 7a, which displays streamlines in the vertical $x = 0$ plane. The down-valley flow existing within the cold-air pool, it behaves like a "flow in a pipe", the height of the pipe being set by that of the cold-air pool. As a result, the down-valley flow speed increases towards the valley exit (see the streamline pattern in Fig. 7a). Figure 6a shows that a jet-like profile develops along the valley axis, which is fully developed at the valley exit, the jet maximum being located at about 40 m above the ground. Whatever the $y-$location, the vertical profile of the flow speed reverses around $z = 1400$ m a.s.l. up to the plateau height, which ensures mass conservation.

As shown in Fig. 6b, the temperature profile displays a very strong ground-based inversion, controlled by radiative cooling at the ground, of about 0.1 K m^{-1} up to the height at which the down-valley flow speed reaches a maximum. This value is an average, over the valley floor and over the first layer, of the absolute temperature vertical gradient at the end of the simulation. The corresponding value of the buoyancy frequency N is very large as well, of about 0.06 rad s^{-1} (close to the ground it may even reach values as high as 0.16 rad s^{-1}, namely 0.7 K m^{-1}). The temperature profile reverses at an altitude around 1150 m a.s.l. and becomes y-independent at the altitude where the down-valley flow speed changes sign (at about 1400 m a.s.l.), slowly converging above towards the initial temperature profile. Figure 6b also shows that the air in the cold-air pool is warmer close to the valley exit than at $y = 3$ km. Indeed, the larger down-valley flow speed at the valley exit results in a larger sensitive heat flux at 9 km than at 3 km; therefore mixing with the air coming from the slopes is stronger at the valley exit than at 3 km (Arduini et al., 2016, showed that there is very little contribution from subsidence).

Fig. 6b shows that the buoyancy frequency in the cold-air pool is larger at $y = 9$ km than at $y = 3$ km, because of the decrease in the cold-air pool height. This is attested in Fig. 7a below, which displays streamlines inside the valley during the quasi-steady regime, recalling that streamlines are also lines of constant potential temperature in this regime if cooling effects are neglected. Figure 6b also shows that N displays vertical oscillations, attesting again to the presence of internal gravity waves. The vertical wavelength is about 100 m in the cold-air pool, consistent with N being ten times larger in the cold-air pool than above the valley (using Fig. 5 to estimate the vertical wavelength above the valley and the dispersion relation of internal gravity waves, the wave frequency being known).

As indicated in Fig. 6b, three layers can be defined along the vertical. These layers will help, in Sect. 4, to characterize the transport properties of the flow. The first layer extends from the ground to the height of the jet maximum (about 40 m above ground level); the second layer surmounts the first layer and extends up to the height of the reversal of the temperature, namely the location at which dT/dz vanishes, at about 1150 m a.s.l.; the third layer extends from the top of the second layer to the height where the down-valley flow speed reverses, at about 1400 m a.s.l.

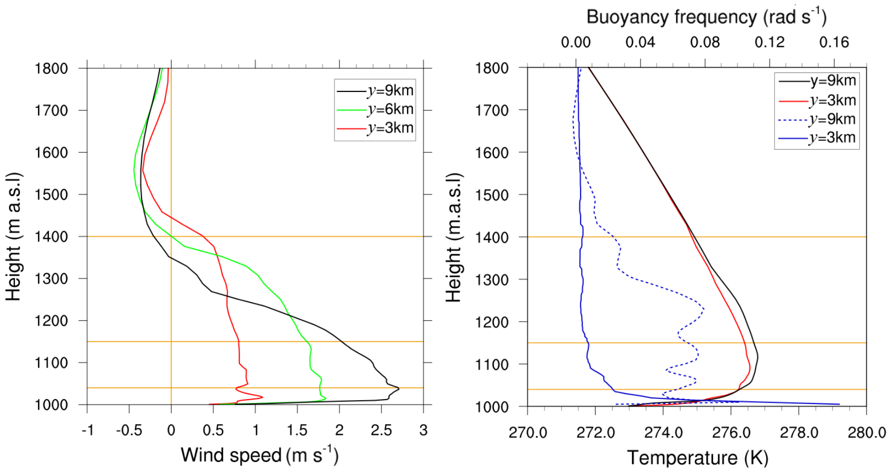

(a) (b)

Fig. 6 Vertical profiles of the down-valley flow speed (a) and of the absolute temperature (b) averaged over the valley floor at different positions along the valley axis, at t = 360 min. Blue lines in b) correspond to the buoyancy frequency at 3 km (solid line) and 9 km (dashed line) from the beginning of the valley averaged over the last hour of simulation. The horizontal orange lines indicate the top of the different layers defined in Sect. 3.3. Results are shown for simulation S1.

3.4 Regions of Turbulence

The identification of the regions where turbulence occurs is an essential step in the understanding of the passive scalar behaviour. Turbulence kinetic energy (TKE) is a good indicator of turbulence and contours of TKE for S1 are displayed in a vertical plane containing the valley axis in Fig. 7a; a zoom over the first 50 m above the valley floor is shown in Fig. 7b.

The development of the down-valley flow displayed in Fig. 6a is reminiscent of that of a low-level jet during the evening transition in a stably stratified atmosphere (e.g. Banta et al., 2003), the temporal development of the low-level jet becoming here a spatial development along the y-direction. As shown by several authors (see Banta et al., 2003, and references therein), turbulence is generated in the layer between the ground and the maximum of the low-level jet, as a result of the strong shear in the jet. Figure 7b shows that this is also the case for simulation S1.

Turbulent regions of a flow can be identified using the local Richardson number,

$$Ri = \frac{\frac{g}{\theta_{v,ref}} \frac{\partial \langle \theta \rangle}{\partial z}}{\left(\frac{\partial \langle U \rangle}{\partial z}\right)^2 + \left(\frac{\partial \langle V \rangle}{\partial z}\right)^2}. \tag{4}$$

In Eq. 4, the $<>$ symbol refers to a spatial average over the valley floor and a temporal average over the last 30 minutes of the simulation. For a steady parallel shear flow in a stably stratified fluid, a necessary condition for instability is $Ri < 1/4$ somewhere in the flow (see Drazin and Reid, 1982). This criterion is actually a good indicator of turbulent regions for any shear flow and is widely used in the literature. Figure 7b shows that the condition $Ri < 1/4$ is satisfied below the jet maximum. We note that the TKE value is of the order of 0.1 m^2 s^{-2}, which is comparable to the lowest values recorded in the field experiments reported in Banta et al. (2003).

Figure 7a displays another turbulent region, which is associated with the upper part of the down-valley flow in the cold-air pool. The streamlines show that a strong shear exists there, as evidenced by a local Richardson number smaller than $1/4$ and, especially, by TKE values being up to seven times larger than those below the jet maximum.

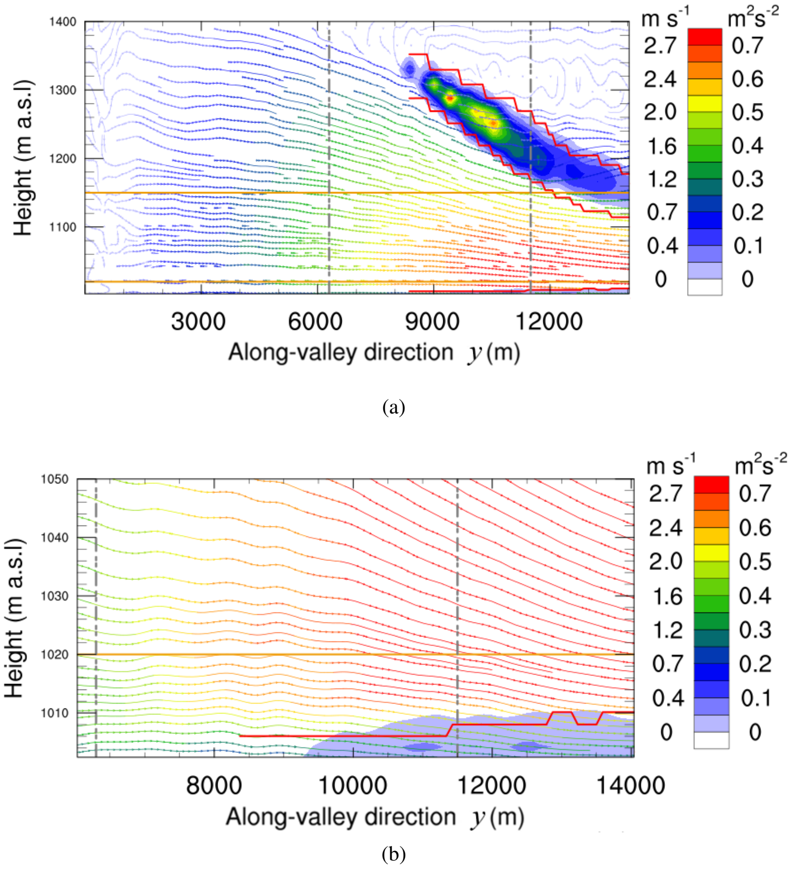

Fig. 7 (a) Contour plot of the turbulent kinetic energy (TKE) (with values indicated in the right column of the colour map) overlaid with streamlines along the valley axis at 360 minutes into the simulation. The colours along the streamlines refer to values of the down-valley flow speed (which are indicated in the left column of the colour map). The regions where Ri, defined by Eq. 4, is less than $1/4$ are bounded by red lines. (b) Zoom of frame (a) over the TKE region close to the bottom. Results are shown for simulation S1.

Apart from these two turbulent regions, the flow can be considered as laminar, with Ri ~ 10. This implies that the flow below the jet maximum is decoupled from the flow above it, as already noted in Cuxart and Jiménez (2007) for the case of a downslope flow over a gentle slope.

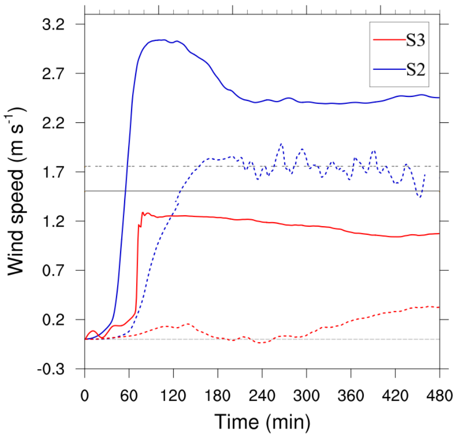

Fig. 8 Solid lines: time series of the downslope flow speed U_s at $y = 6$ km, $z = 20$ m above the ground level and $x = 2500$ m for simulations S2 (blue) and $x = 3000$ m for S3 (red). The $x-$position is located just outside (and above) the region along the slope where the hydraulic jump forms. Dashed lines: times series of the down-valley flow speed V at $y = 6$ km, averaged over the valley floor for simulations S2 (blue) and S3 (red). Grey lines indicate the values of U_s (solid line) and V (dashed line) in S1 once the quasi-steady state is reached, averaged from 180 to 360 min. The dotted horizontal light-grey line is the zero speed line.

3.5 Sensitivity Study

The impact of the slope angle and of the value of the buoyancy frequency on the dynamics of the flow described in the previous section are now briefly analyzed, based on the results of simulations S2 and S3 (see Table 1).

Figure 8 displays time series of the downslope flow speed U_s and of the down-valley flow speed V at $y = 6$ km for simulations S2 and S3. Despite the gentler slope in S2 than in S1, implying that the along-slope component of the gravity vector is smaller in the former case than in the latter case, U_s reaches a higher quasi-steady value in S2 than in S1. This behaviour can be explained as follows (Zardi and Whiteman, 2013). The sensible heat flux close to the slope leads to a cooling of the fluid layer and, therefore, to its downward motion along the slope. For the same atmospheric conditions, an air parcel travelling over a longer slope (as in S2) will loose more heat than along a shorter slope (as in S1) for a given difference in altitude travelled by the fluid parcel. The speed at the bottom of the slope reached by the fluid parcel will therefore be larger for the shallower slope (S2) than for the steeper slope (S1) as the plateau height is the same in both simulations. In the present case, the quasi-steady value of U_s for S2 is about 50% larger than that for S1 (compare Fig. 3a and Fig. 8).

The larger U_s speed in S2 leads to a greater mass flux of a slightly colder air mass. However, since the T2 topography is associated with a larger valley volume than the T1 topography, the height of the cold-air pool is eventually smaller in S2 than in S1 (compare Fig. 7a and 10a). As a result, the maximum value of the jet speed at the valley exit is larger in S2 than in S1 (compare Fig. 6a and 9a), but the average value over the valley floor is found to be similar (see Fig. 8).

As for S1, three layers can be defined for S2 from the vertical profiles of V and the temperature (see Fig. 9a): a first layer of height 20 m limited by the height of the jet maximum associated with a layer-averaged temperature gradient of about 0.1 $\mathrm{K\,m^{-1}}$, a second layer

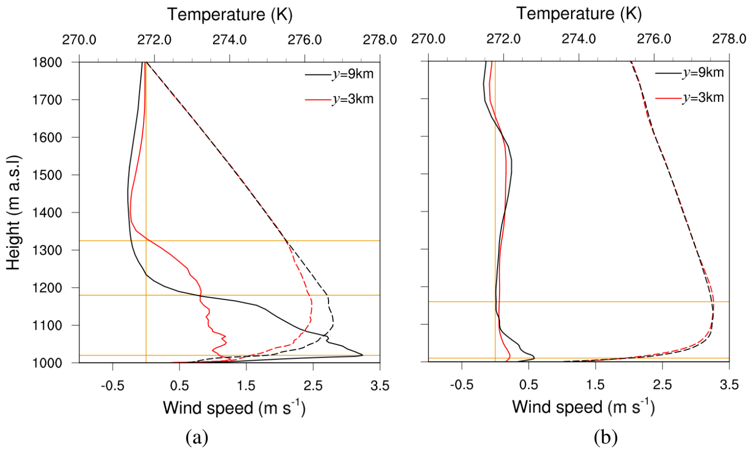

Fig. 9 Vertical profile of the down-valley flow speed (solid lines) and of the temperature (dashed lines) at $t = 360$ min, for $y = 3$ km (red colour) and $y = 9$ km (black colour). Horizontal orange lines denote the height of the layers detected inside the flow. a) Simulation S2 and b) Simulation S3. Data were taken at the valley centre in both simulations.

limited by the top of the ground-based inversion at about 1180 m a.s.l., and a third layer up to the top of the cold-air pool at 1320 m a.s.l.

The turbulent regions of the flow are identified in Fig. 10a by contours of TKE and the line associated with the critical value of $1/4$ for the Richardson number. The same two regions as in S1 are recovered, below the jet maximum and at the top of the cold-air pool near the valley exit, where the strongest vertical shear of the down-valley flow speed occurs. However, as opposed to S1, the largest TKE values are encountered here close the ground. These values are about twice larger than in S1, consistent with the larger down-valley flow speed maximum.

The doubling of the value of the buoyancy frequency for S3 has a very strong impact on the valley-wind system. Theoretical models of the downslope flow speed predict that this speed is inversely proportional to the buoyancy frequency (see Prandtl, 1952; McNider, 1982), implying that it should be weaker for S3 than for S1. Fig. 8 shows that this is the case, U_s for S3 being 50% smaller than for S2 at the positions considered in this figure. The mass flux associated with the downslope flow is therefore smaller for S3 than for S1 and the topography being the same, the height of the cold-air pool is smaller for S3 than for S1 as well. The cold-air pool in S3 actually coincides with the ground-based inversion (see Fig. 9b), implying that the temperature profile hardly varies along the valley axis. As a result, the pressure difference between the valley and the plain is very small and a weak down-valley flow develops, whose maximum speed reaches at most 0.5 $\mathrm{m\,s^{-1}}$ at the valley exit. Only two layers can be identified from the vertical profiles of the down-valley flow speed and the absolute temperature. The first layer is the ground-based inversion and is very thin, about 10-m high, and is associated with the same very strong gradient of temperature as for S1 and S2; the second layer extends up to about 1150 m a.s.l. As expected (see Fig. 10b), the down-valley flow speed for S3 does not exhibit any turbulent region and remains localized in a layer close to the ground, about 10-m high, with a value smaller than 1 m $\mathrm{s^{-1}}$.

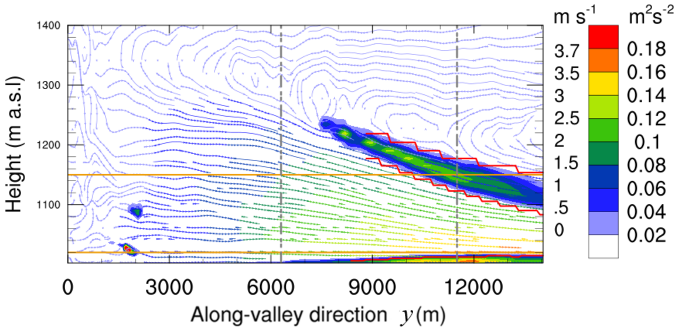

(a)

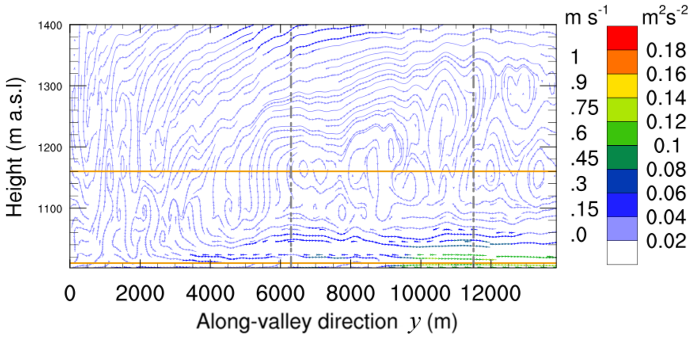

(b)

Fig. 10 Same as Fig. 7a: (a) for simulation S2; (b) for simulation S3.

4 Properties of the Tracer Concentration Field

All tracers were emitted 150 min after the initial time, when the along-valley flow is fully developed, to analyze the impact of this flow and of the stable stratification on the tracer behaviour. During the first hour of simulation indeed, a vertical motion is induced inside the valley by the convergence of the downslope flows, which would transport the tracer upwards inside the valley volume if emission were imposed from the initial time.

We recall that the tracers are emitted in four zones along the valley axis, each of them covering a surface area equal to the valley width along the x-direction (1440 m) and extending over 1080 m along the y-direction; for each zone, emission occurs at the valley floor and at three different heights above it (see Table 2). These heights have been selected so as to be located inside the highest layer identified in Sect. 3.4 for S1, of altitude 1400 m a.s.l.

4.1 Overall Behaviour of the Tracer Concentration Along the Valley Axis

Contours of the tracer concentration are displayed in Fig. 11 at 360 min into the simulation in the vertical plane $x = 0$ (containing the valley axis) for S1 and S3, along with streamlines. The emission zone is Z_1 in frames a) to h), with the tracer being emitted at the four different levels mentioned above, and Z_4 in frames (i) and (j).

The tracer is advected by the velocity field, which is mainly contributed by the down-valley flow in the $x = 0$ plane (there is no cross-valley flow in that plane, by symmetry, and the vertical velocity is of much weaker amplitude than the down-valley flow speed). The valley-wind system being quasi-steady once the down-valley flow has fully developed (see Section 3.1), tracer contours closely follow the streamlines of that flow. Since this flow is laminar apart from the two turbulent regions identified in Sect. 3.4 for S1, one expects the tracers emitted at different heights to remain decoupled while being advected toward the valley exit; the latter point is clearly illustrated in Fig. 11.

For S1 (left column of Fig. 11), striking additional features should be noted. The tracer released at the ground (see Fig. 11a) spreads vertically but remains trapped below the first maximum of the down-valley flow speed. In a real valley during wintertime where particulate air pollution is mainly contributed by PM_{10}, assuming the passive scalar behaviour is valid, the latter result could explain the height above the valley floor over which pollution levels are highest during nighttime. Figure 11a also shows that the concentration decreases as the valley exit is approached. This results from the tracer concentration to be inversely proportional to the down-valley flow speed (which increases toward the valley exit as already shown), as discussed in the next section.

When emission occurs within the cold-air pool (see Figs. 11a, 11c and 11e), the tracer is advected towards the valley exit. However, the decrease of the concentration along the valley axis implies that, depending upon the emission sources, the superposition of the different tracers at the valley exit may not lead to a concentration higher than inside the valley, closer to the emission source.

When the tracer is emitted at the top of the cold-air pool where the down-valley flow speed is very weak (see Fig. 11g), the tracer remains localized at the emission location, as expected, apart from a weak vertical diffusion.

The purpose of Fig. 11i is to illustrate the presence of the return flow above the cold-air pool. Indeed, at 360 min, the tracer has moved towards the beginning of the valley, as opposed to the tracers at lower altitudes. This figure also shows that the higher is the tracer release altitude the stronger is the vertical diffusion for $y = 3$ km, because the local buoyancy frequency, that is the stratification level, decreases with height (see Fig. 6b for $y = 3$ km, the behaviour being similar for $y = 6$ km).

As for S3 (see right column of Fig. 11), the passive tracer remains trapped within its emission zone because of the very weak down-valley flow speed, with a weak dispersion along the vertical. As a result, higher concentration levels than for S1 are reached locally at 360 min. This simulation S3 will not be further considered in the remainder of this section.

4.2 Temporal Evolution of the Tracer Flux

The total tracer flux across a vertical cross-section of the valley located 2 km downstream from the centre of an emission zone (Z_1, Z_2 or Z_3) is displayed in Fig. 12 for S1 and S2. This cross-section, denoted Σ, extends from the valley floor to the top of the cold-air pool, whose height above the valley floor is denoted z_{CAP}.

Since the tracers are released 150 min after the initial time, the tracer flux in Fig. 12 starts to grow from this time on. More precisely, the growth starts when the tracer reaches the vertical area Σ and the smaller is the down-valley flow speed the later this growth occurs, namely the closer to the beginning of the valley is the emission zone. The tracer flux eventually reaches the same quasi-steady value (apart from oscillations associated with internal gravity waves) whatever the (y-)position of Σ.

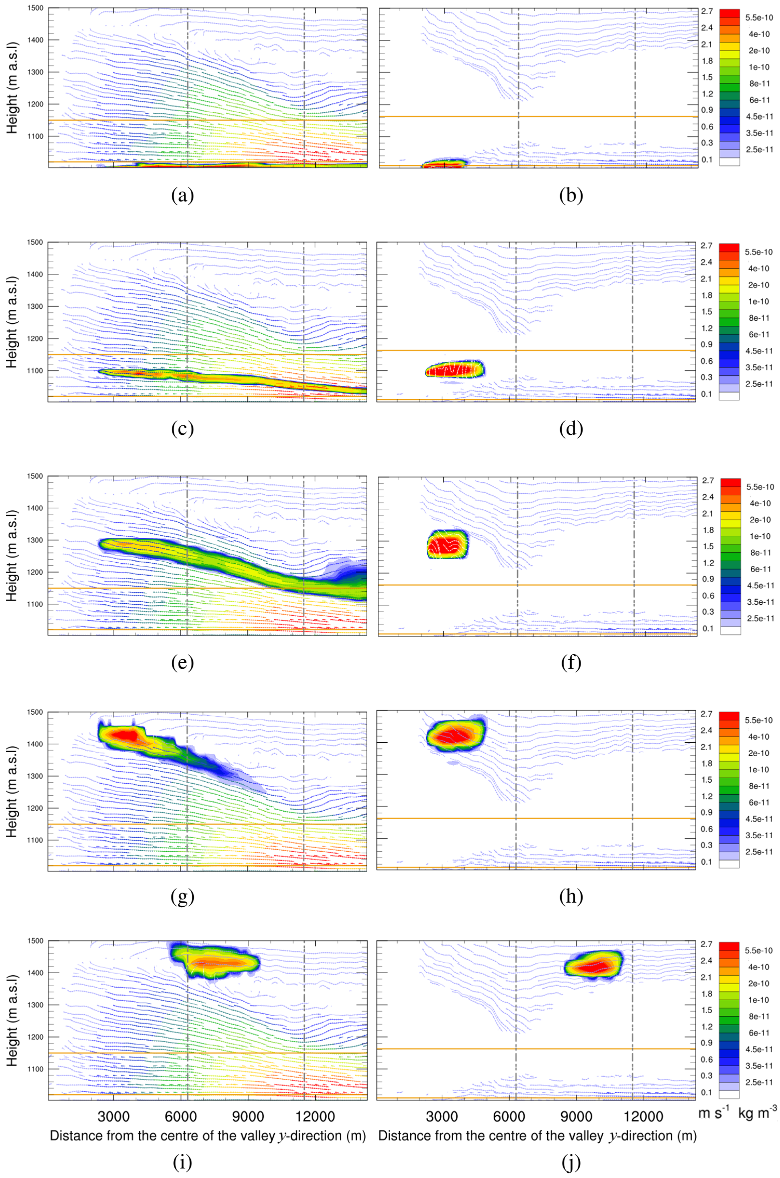

Fig. 11 Contour plots of tracer concentration overlaid with streamlines in the $x = 0$ vertical plane at t = 360 min for simulation S1 (left column) and S3 (right column). In panels a) to h), tracers were released in zone Z_1 at different heights: a) and b) surface level ($TrS1_{1,1}$ and $TrS3_{1,1}$), c) and d) 100 m above the ground ($TrS1_{1,2}$ and $TrS3_{1,2}$), e) and f) 280 m above the ground ($TrS1_{1,3}$ and $TrS3_{1,3}$), g) and h) 415 m above the ground ($TrS1_{1,4}$ and $TrS3_{1,4}$). Panels i) and j) correspond to $TrS1_{4,4}$ and $TrS3_{4,4}$, respectively, released in zone Z_4 and at 415 m above the ground level. The two lower layers identified in Sect. 3.3 for S1 and in Sect. 3.5 for S3 are indicated with an orange horizontal line for each simulation.

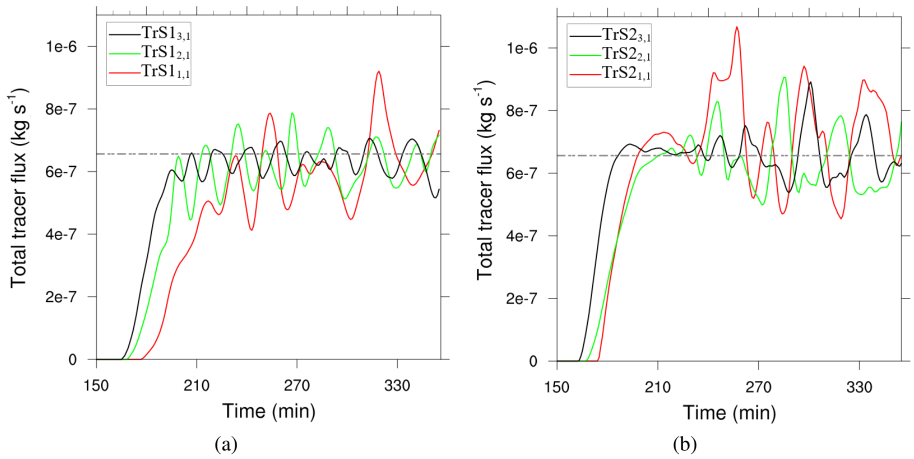

Fig. 12 a) Time series of the total tracer flux ($TrS1_{1,1}$, $TrS1_{2,1}$ and $TrS1_{3,1}$) through the cross-sectional area of the valley Σ located at 2 km from the centre of a tracer emission zone for S1. b) Same as a) for S2. The area Σ extends vertically from the valley bottom to the top of the cold-air pool z_{CAP}. The horizontal dashed line indicates the value of the emission rate Q over each emission zone.

The fact that the same quasi-steady value is reached for S1 and S2 can be easily explained by considering the equation for the tracer concentration,

$$\frac{\partial C}{\partial t} + \mathbf{u}.\nabla C = \nabla.(\kappa \nabla C) + q, \tag{5}$$

where C is the tracer concentration, $\mathbf{u} = (u, v, w)$ is the velocity field and κ is the turbulent diffusivity of the tracer (equal to the thermal diffusivity given by the model of Deardorff, 1980); q is the local emission rate, whose surface integral over a zone Z_i, whatever i, is equal to Q. Assuming that a steady state has been reached, that the flow is incompressible and ignoring diffusive effects yields the simplified equation,

$$\nabla.(\mathbf{u}C) = q. \tag{6}$$

We consider the small volume $d\mathscr{V}$ delimited by the slopes of the valley along the x-direction, by Σ-sections located at positions y and $y + dy$ inside the valley but outside an emission zone and by the valley floor and the cold-air-pool height along the z-direction. Integrating over $d\mathscr{V}$ and using the divergence theorem yields

$$\int_{\Sigma} vC\, dx\, dz = \text{constant}, \tag{7}$$

since there is no tracer at the top of the cold-air pool and no emission inside $d\mathscr{V}$. The constant value is the total emission rate over a zone Z_i, equal to Q,

$$\int_{\Sigma} vC dx dz = Q, \tag{8}$$

which simply expresses the conservation of the tracer emitted at the valley floor. As shown in Fig. 12, the total flux over Σ is the same for S1 and S2 since the emission rate is the same (but the areas Σ are different). Figure 12 also shows that the tracer flux displays marked oscillations, which are discussed below. Note that the along-valley velocity component v coincides with the down-valley flow speed V since the sign of v is positive at all times. In the following, for consistency with the rest of the paper, v will therefore be referred to as V.

It is useful at this stage to express Eq. 8 in terms of the mean values of C and V over the area Σ. Denoting the average value over Σ by $<>_\Sigma$, the integral $\int_\Sigma VC dx dz$ is equal to $\Sigma < VC >_\Sigma$. Assuming that the fluctuations of V and C are much smaller than their average values, $< VC >_\Sigma$ can be written as $< V >_\Sigma < C >_\Sigma$. This assumption is actually approximately satisfied: the ratio $\beta =< VC >_\Sigma / < V >_\Sigma < C >_\Sigma$ ranges from $\beta \approx 2$ for $y = 3$ km to $\beta \approx 1.3$ for $y = 9$ km. Equation 8 thus becomes:

$$< C >_\Sigma = \frac{Q}{\beta \Sigma < V >_\Sigma}, \tag{9}$$

$< C >_\Sigma$ and $< V >_\Sigma$ being a function of y.

Since the tracer remains trapped in the bottom layer identified in section 3.3 for S1 and in section 3.5 for S2, the integral of C over Σ is actually equal to the integral of C over the area, denoted $\mathscr{A}$, defined by this bottom layer along the vertical and by the valley cross-section in the horizontal. The identity $\mathscr{A} < C >_\mathscr{A} = \Sigma < C >_\Sigma$ implies that Eq. 9 can also be written as:

$$< C >_\mathscr{A} = \frac{Q}{\beta \mathscr{A} < V >_\Sigma}. \tag{10}$$

Equation 9 (or equivalently Eq. 10) recovers a well-known result for so-called "trapped plumes" in a stably-stratified fluid (see Beychok, 1995, chp 8). Equation 9 also qualitatively accounts for the behaviour of the tracer concentration in Fig. 11: since the down-valley flow speed increases with y, the concentration should decrease towards the valley exit, which is indeed what is observed. A more precise prediction of the tracer concentration is derived in section 4.4 below.

4.3 Temporal Evolution of the Tracer Concentration

The temporal evolution of the tracer flux integrated over the area Σ displayed in Fig. 12 shows marked temporal oscillations induced by the internal gravity wave field identified in section 3.2. The tracer being advected by the down-valley flow, its concentration is expected to oscillate as well but it is useful to quantify the magnitude of these oscillations. For this purpose, the concentration of the tracers released at the ground level from the three zones Z_i, $1 \leq i \leq 3$, is displayed in Fig. 13 for S1 and S2, at a position $y_i = 2$ km from the centre of the Z_i emission zone. The concentration is averaged over the area $\mathscr{A}$ (or, equivalently, Σ).

Once the tracer emitted from a given zone Z_i has reached the counterpart y_i position, the concentration at that position reaches a quasi-steady value controlled by that of the down-valley flow speed at y_i. This value is higher close to the beginning of the valley and lower close to the valley exit, consistent with equation 10. The striking feature of Fig. 13 lies in the amplitude of the oscillations of the concentration. For the tracer emitted from zone Z_1 in S1 for instance ($TrS1_{1,1}$), the concentration may reach values as high as 50% of the mean value. This effect is likely to occur in a real valley and should not be disregarded. From an operational point of view indeed, the pollutant concentration is usually averaged over one hour, possibly smoothing out those large fluctuations.

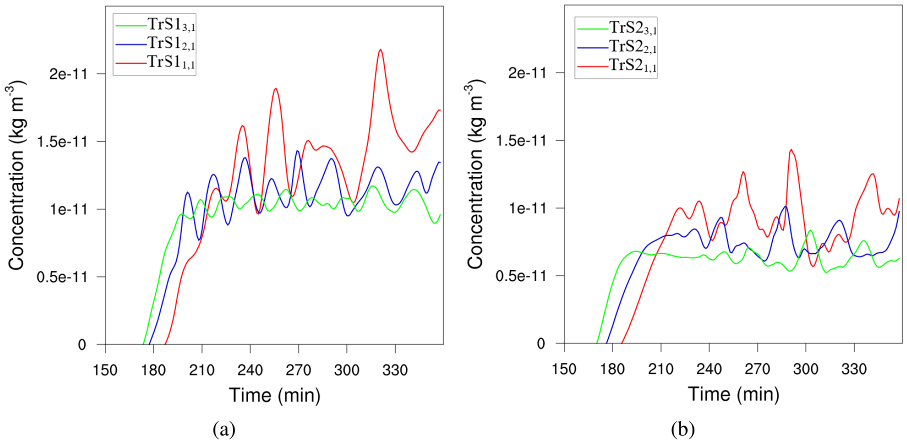

Fig. 13 (a) Time series of the tracer concentration averaged over the area $\mathscr{A}$ (defined in Section 4.2) for $TrS1_{1,1}$, $TrS1_{2,1}$ and $TrS1_{3,1}$. (b) Same as (a) for S2. Each curve is plotted at two kilometres from the centre of the tracer emission zone. Emission starts at 150 min.

4.4 Evolution of the Tracer Concentration Along the Valley Axis

The tracer concentration averaged over the area $\mathscr{A}$ is plotted versus the along-valley direction y at $t = 300$ min in Fig. 14, for the tracers emitted at ground level in S1.

The figure displays two striking features. As regards the concentration field, a similar behaviour is observed whatever the emission zone, that is: the concentration increases with y inside the emission zone, at a rate that is inversely proportional to the local down-valley flow speed, and next decreases with the same law whatever the emission zone, leading to similar values of the $\mathscr{A}$-averaged concentrations emitted from the different zones. As for the down-valley flow speed, it displays a remarkable linear growth before saturating when reaching the plain.

This linear growth can be predicted by expressing the conservation of mass in the cold-air pool inside the valley, once the down-valley flow has developed. We consider again the small volume $d\mathscr{V}$, noticing that Σ depends upon y because of the decreasing height of the cold air pool inside the valley; more precisely Σ is constant in the plateau region ($0 \le y \le 6$ km) and decreases out of it ($6 \le y \le 11$ km). The mass fluxes across $d\mathscr{V}$, whose sum vanishes by mass conservation, are those across the Σ-sections and across the top of the volume. In the following the density is assumed to be constant. The net flux across the Σ-sections is

$$(\Sigma < V >_\Sigma)(y+dy) - (\Sigma < V >_\Sigma)(y) \approx \frac{\partial(\Sigma < V >_\Sigma)}{\partial y} dy. \tag{11}$$

The flux across the top of the volume is mainly contributed by the downslope flow (see Arduini et al., 2016). The projection of this flux along the vertical direction is thus equal to $-2\overline{U_s}\, h_n \sin\alpha_{\text{CAP}}\, dy$, where h_n is the depth normal to the slope of the downslope flow speed U_s, $\overline{U_s}$ is the average of U_s over h_n and α_{CAP} is the slope angle of the topography at the top of the cold-air pool. Conservation of mass in volume $d\mathscr{V}$ therefore implies that

$$\frac{\partial(\Sigma < V >_\Sigma)}{\partial y} - 2\overline{U_s}\, h_n \sin\alpha_{\text{CAP}} = 0. \tag{12}$$

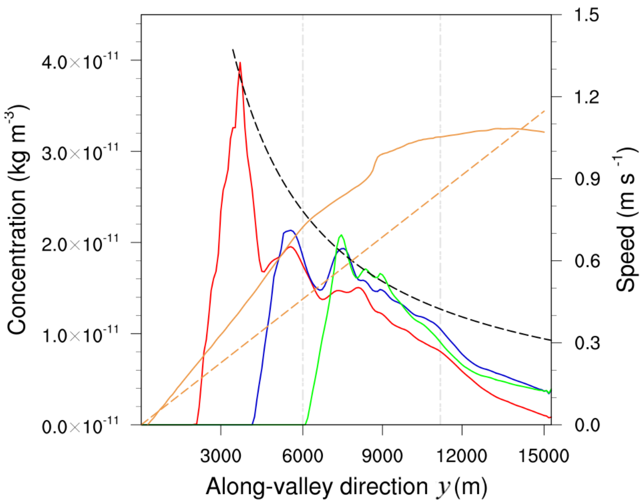

Fig. 14 Tracer concentration averaged over the area $\mathscr{A}$ at t = 300 min versus the along-valley direction, for tracers emitted at the surface level in simulation S1 ($TrS1_{1,1}$, $TrS1_{2,1}$ and $TrS1_{3,1}$). The down-valley flow speed (V) averaged over the area Σ is also displayed at the same time (orange colour). The dashed lines are the theoretical predictions for V (orange dashed line, Eq. 13) and for the concentration (black dashed line, Eq. 15), respectively. The grey vertical lines represent the end of the plateau and of the valley.

Integration of this equation is simple only if $\overline{U_s}$, h_n and α_{CAP} do not depend upon y. This is approximately the case in the plateau region only. In this region, where Σ has a constant value, one gets a simple expression for the Σ-averaged down-valley flow speed, using the boundary condition $< V >_\Sigma = 0$ for $y = 0$:

$$< V >_\Sigma (y) = \frac{2\overline{U_s}\, h_n \sin\alpha_{\text{CAP}}}{\Sigma}\, y. \tag{13}$$

Equation 13 thus predicts that, in the plateau region, the down-valley flow speed averaged over a valley section inside the cold-air pool evolves linearly with y; this is indeed what Fig. 14 shows.

Let us estimate the numerical value of the growth rate predicted by Eq. 13. The expression of the area Σ is

$$\Sigma = 2z_{\text{CAP}}\left(L_x + S_x^{\text{CAP}}\right) - H\left(S_x^{\text{CAP}} - \frac{S_x}{\pi}\sin\left(\pi\frac{S_x^{\text{CAP}}}{S_x}\right)\right), \tag{14}$$

where the length scales L_x, H and S_x have been defined in section 2.2; S_x^{CAP} is defined such that $2\left(L_x + S_x^{\text{CAP}}\right)$ is the horizontal extent of the cold-air pool upper surface; from the expression of the topography (Eq. 2), $S_x^{\text{CAP}} = (S_x/\pi)\,\text{acos}(1 - 2z_{\text{CAP}}/H)$. With $\overline{U_s} \approx 2.5$ m s^{-1}, $h_n \approx 90$ m, $\alpha = 16.7°$, $L_x = 720$ m (using values from Arduini et al., 2016)) and $z_{\text{CAP}} \approx 400$ m (from section 3.3), the growth rate of $< v >_\Sigma$ is equal to 7.86×10^{-5} s^{-1}. This value is of the same order as that inferred from Fig. 14, equal to $\approx 1.2 \times 10^{-4}$ s^{-1} (the ratio of these two values being ≈ 1.5).

Using Eqs. 10 and 13, we infer the expression for the tracer concentration emitted from a zone Z_i, valid inside the plateau region of the valley and out of Z_i,

$$< C >_{\mathscr{A}} (y) = \frac{\Sigma}{\mathscr{A}} \frac{Q}{\beta\,(2\overline{U_s}\,h_n\,\sin\alpha_{\mathrm{CAP}})} \frac{1}{y}, \tag{15}$$

with Σ defined by Eq. 14. This law is superposed on the evolution of the concentration in Fig. 14a. The area $\mathscr{A}$ is equal to $2L_x h_1$, where $h_1 \approx 20$ m is the height of the first layer. A value of the parameter $\beta = 2$ has been used, implying that the concentration emitted at zone Z_1 is modelled. The agreement can be considered as being quite good.

5 Summary and Conclusions

We have investigated and modelled the impact of a valley-wind system on the night time behaviour of a passive tracer released in an idealized Alpine-type valley. Persistent stable atmospheric conditions are assumed, as they occur in winter during an anticyclonic regime, sometimes leading to a dynamical decoupling between the valley-wind system and the synoptic meteorological fields. This decoupling is imposed here and the case of a simple valley opening on a plain is considered, as in Arduini et al. (2016).

The first part extends the analysis of the valley-wind system proposed in Arduini et al. (2016) when a steady state has been reached. We focus on the down-valley flow dynamics with its impact on tracer transport in mind. We show that the down-valley flow displays oscillations induced by internal gravity waves emitted, via a hydraulic jump, by the downslope flow when reaching the valley floor (or its level of neutral buoyancy). The down-valley flow is however weakly turbulent, as it exhibits turbulence in two regions only: close to the valley floor, within a shallow layer (≈ 20 m) extending from the ground to the first maximum of this flow, which behaves like a jet; and at the top of the cold-air pool close to the valley exit, where the flow accelerates because of the decreasing height of the cold-air pool. The down-valley flow is elsewhere laminar because of the stable stratification. When averaged horizontally over the valley floor and vertically over the height of the cold-air pool, an area denoted by Σ in the paper, the down-valley flow speed displays a remarkable linear profile inside the valley, which can be modelled analytically using mass conservation within the cold-air pool; this is Eq. 13.

Passive tracers are emitted at the beginning of the steady regime and display several striking features. Firstly, the tracer emitted at the ground remains trapped at all times inside the shallow layer extending up to the jet speed maximum. As a consequence, and because the flow is laminar elsewhere (except in the second region detected close to the valley exit), tracers emitted above that bottom layer at different altitudes are advected towards the valley exit but do not meet. Evidence of this vertical decoupling in a real valley under stable wintertime conditions is provided in Fig. 15. The height of the jet-speed maximum may account in this real case for the height over which pollutants are trapped, a conjecture which would need to be tested.

Outside its emission zone, the passive tracer averaged over the trapping region close to the ground, an area denoted by $\mathscr{A}$, displays a decaying law along the valley axis. This law can be modelled from the conservation of the tracer flux in the down-valley direction and the linear behaviour of the down-valley flow speed; this is Eq. 15. The concentration thus decreases as $1/y$ at a given time, where y is the along-valley coordinate. As a consequence, the total concentration at the valley exit, where the various valley-floor emissions superpose, may not be larger than inside the valley close to an emission source.

At a given location inside the valley, the concentration averaged over the area $\mathscr{A}$ displays strong temporal oscillations, induced by the down-valley flow, which may reach 50% of the mean (over time) value of the concentration. If occurring in a real valley, this would imply that time-averaged values in an urbanized valley may disguise high instantaneous, and potentially harmful, values.

Even if several conclusions regarding tracer transport in a real valley can be proposed from the present work, the highly idealized configuration considered here requires that the impact of main topographical features on the transport of tracers be taken into account, such as a change in the valley width along the valley axis (as done by Arduini et al., 2017), a non flat valley floor or tributary valleys.

Fig. 15 View of the Grenoble valley during an anticyclonic regime on December 18, 2016. Vertically decoupled cloud layers attest of the strong stratification of the atmospheric boundary layer (photo by C. Staquet).

Acknowledgements The PhD work of J. Quimbayo is supported by the Colombian Administrative Department of Science, Technology and Innovation (COLCIENCIAS). Numerical simulations were run on the French national HPC facilities at CINES.

References

Anquetin S, Guilbaud C, Chollet JP (1999) Thermal valley inversion impact on the dispersion of a passive pollutant in a complex mountainous area. Atmos Environ 33(24):3953–3959

Arduini G, Staquet C, Chemel C (2016) Interactions between the nighttime valley-wind system and a developing cold-air pool. Boundary-Layer Meteorol 161(1):49–72

Arduini G, Chemel C, Staquet C (2017) Energetics of deep alpine valleys in pooling and draining configurations. J Atmos Sci 74 (7):2105–2124

Banta RM, Pichugina YL, Newsom RK (2003) Relationship between low-level jet properties and turbulence kinetic energy in the nocturnal stable boundary layer. J Atmos Sci 60(20):2549–2555

Beychok M (1995) Fundamentals of stack gas dipersion. M.R. Beychok ed., Irvine, California

Brulfert G, Chemel C, Chaxel E, Chollet J (2005) Modelling photochemistry in alpine valleys. Atmos Chem Phys 5(9):2341–2355

Burns P, Chemel C (2014) Evolution of cold-air-pooling processes in complex terrain. Boundary-Layer Meteorol 150(3):423–447

Chemel C, Burns P (2015) Pollutant dispersion in a developing valley cold-air pool. Boundary-Layer Meteorol 154(3):391–408

Chemel C, Staquet C, Largeron Y (2009) Generation of internal gravity waves by a katabatic wind in an idealized alpine valley. Meteorol Atmos Phys 103(1-4):187–194

Cuxart J, Jiménez M (2007) Mixing processes in a nocturnal low-level jet: An les study. J Atmos Sci 64(5):1666–1679

Deardorff JW (1980) Stratocumulus-capped mixed layers derived from a three-dimensional model. Boundary-Layer Meteorol 18(4):495–527

Drazin P, Reid W (1982) Hydrodynamic stability. Cambridge University Press, Cambridge

Dudhia J (1989) Numerical study of convection observed during the winter monsoon experiment using a mesoscale two-dimensional model. J Atmos Sci 46:3077–3107

Jiménez PA, Dudhia J, González-Rouco JF, Navarro J, Montávez JP, García-Bustamante E (2012) A revised scheme for the wrf surface layer formulation. Mon Weather Rev 140(3):898–918

Klemp J, Dudhia J, Hassiotis A (2008) An upper gravity-wave absorbing layer for nwp applications. Mon Weather Rev 136(10):3987–4004

Lang M, Gohm A, Wagner J (2015) The impact of embedded valleys on daytime pollution transport over a mountain range. Atmos Chem Phys 15(20):11,981–11,998

Lareau NP, Crosman E, Whiteman CD, Horel JD, Hoch SW, Brown WO, Horst TW (2013) The persistent cold-air pool study. Bull Am Meteorol Soc 94(1):51–63

Largeron Y, Staquet C (2016) The atmospheric boundary layer during wintertime persistent inversions in the Grenoble valleys. Frontiers in Earth Science 4:70

Lehner M, Gohm A (2010) Idealised simulations of daytime pollution transport in a steep valley and its sensitivity to thermal stratification and surface albedo. Boundary-Layer Meteorol 134(2):327–351

McNider RT (1982) A note on velocity fluctuations in drainage flows. J Atmos Sci 39(7):1658–1660

Mlawer EJ, Taubman SJ, Brown PD, Iacono MJ, Clough SA (1997) Radiative transfer for inhomogeneous atmospheres: RRTM, a validated correlated-k model for the longwave. J Geophys Res 102:663–682

Peckham SE, Grell GA, McKeen SA, Barth M, Pfister G, Wiedinmyer C, Fast JD, Gustafson WI, Ghan SJ, Zaveri R, et al. (2012) WRF/Chem Version 3.3 User's Guide. US Department of Commerce, National Oceanic and Atmospheric Administration, Oceanic and Atmospheric Research Laboratories, Global Systems Division

Prandtl L (1952) Essentials of fluid dynamics: with applications to hydraulics, aeronautics, meteorology and other subjets (English translation). Blackie & Son

Rampanelli G, Zardi D, Rotunno R (2004) Mechanisms of up-valley winds. J Atmos Sci 61(24):3097–3111

Rendón AM, Salazar JF, Palacio CA, Wirth V, Brötz B (2014) Effects of urbanization on the temperature inversion breakup in a mountain valley with implications for air quality. J Appl Meteorol Climatol 53(4):840–858

Renfrew IA (2004) The dynamics of idealized katabatic flow over a moderate slope and ice shelf. Q J R Meteorol Soc 130:1023–1045

Schmidli J, Rotunno R (2015) The quasi-steady state of the valley wind system. Frontiers in Earth Science 3:79

Scotti A, Meneveau C, Lilly DK (1993) Generalized smagorinsky model for anisotropic grids. Physics of Fluids A: Fluid Dynamics (1989-1993) 5(9):2306–2308

Silcox GD, Kelly KE, Crosman ET, Whiteman CD, Allen BL (2012) Wintertime pm 2.5 concentrations during persistent, multi-day cold-air pools in a mountain valley. Atmos Environ 46:17–24

Wagner J, Gohm A, Rotach M (2014) The impact of valley geometry on daytime thermally driven flows and vertical transport processes. Q J R Meteorol Soc 141(690):1780–1794

Whiteman CD, Pospichal B, Eisenbach S, Weihs P, Clements CB, Steinacker R, Mursch-Radlgruber E, Dorninger M (2004) Inversion breakup in small rocky mountain and alpine basins. J Appl Meteorol 43(8):1069–1082

Whiteman CD, Hoch SW, Horel JD, Charland A (2014) Relationship between particulate air pollution and meteorological variables in utah's salt lake valley. Atmos Environ 94:742–753

Zardi D, Whiteman CD (2013) Diurnal mountain wind systems. In: Chow FK, De Wekker SF, Snyder BJ (eds) Mountain Weather Research and Forecasting: Recent Progress and Current Challenge, Springer, Springer: Berlin, pp 35–119